Atomistic mesh generation for the simulation of nanoscale metal-oxide-semiconductor field-effect transistors

M. Aldegunde,* Natalia Seoane, and A. J. García-Loureiro
Departamento de Electrónica y Computación, Universidad de Santiago de Compostela, 15782 Santiago de Compostela, Spain

P. V. Sushko and A. L. Shluger
Department of Physics & Astronomy, University College London, London WC1E 6BT, United Kingdom

J. L. Gavartin
Accelrys, 334 Cambridge Science Park, Cambridge, CB4 0WN, United Kingdom

K. Kalna and A. Asenov
Department of Electronics & Electrical Engineering, University of Glasgow, Glasgow G12 8LT, United Kingdom
(Received 23 November 2007; revised manuscript received 10 March 2008; published 8 May 2008)

We present a methodology for the finite-element discretization of nanoscaled semiconductor devices with atomic resolution. The meshing strategy is based on the use of patterns to decompose the unit cell of the underlying crystallographic structures producing unstructured tetrahedral meshes. The unit cells of the bulk semiconductors and, more importantly, of the interfaces between the substrate and the gate dielectric have been extracted from classical molecular dynamics and density functional theory simulations. A Monte Carlo approach has been then used to place the dopants in nodes of the crystal, replacing silicon atoms. The thus created "atomistic" meshes are used to simulate an ensemble of microscopically different double-gate Si metal-oxide-semiconductor field-effect transistors and the transition region at the Si/SiO_2 interface. In addition, a methodology to approximate amorphous dielectrics is also presented.

DOI: 10.1103/PhysRevE.77.056702 PACS number(s): 02.70.−c, 85.30.De

I. INTRODUCTION

Advances in fabrication technology have enabled the scaling of semiconductor devices to dimensions with countable number of atoms of the constituent materials when the position of each individual atom affects the device characteristics [1]. At the end of the current edition of the International Technology Roadmap for Semiconductors [2], transistors with physical gate lengths as small as 5 nm are expected to be in mass production. At such device dimensions, there would be space for only ten silicon unit cells along the transport direction. Therefore, high-quality mesh generators are required in order to accurately resolve atomic-scale effects in the simulation of complementary metal-oxide-semiconductor (CMOS) devices [3] with nanometer dimensions. At these dimensions, the discreteness of matter begins to play an important role and strongly affects device characteristics [4]. For example, the effects of random dopants will introduce variations in the behavior of semiconductor devices [4–6]. However, in these studies, to our best knowledge, the exact positions of the dopants in the silicon crystal lattice have not been accurately resolved. Figure 1 illustrates that positions of individual atoms in a 10-nm-gate-length double-gate (DG) metal-oxide-semiconductor field-effect transistor (MOSFET) have to be taken into account in realistic simulations as an accurate description of the physical quantities of interest, such as potential and carrier densities, requires a precise calculation of the Coulomb interaction. While the atomic structure of the periodic crystal lattice of silicon has a well-known symmetry, the construction of a good quality mesh for amorphous materials such as silica (a-SiO_2) (Fig. 2) [7] is very challenging. The challenge especially occurs at the Si/SiO_2 interface even for a simple-crystalline structure of SiO_2 (α-quartz) as shown in Fig. 3.

In this paper, we present a tetrahedral mesh generation framework allowing one to reproduce the exact position of the atoms in a semiconductor device. We apply this framework to two material systems: (i) a silicon semiconductor

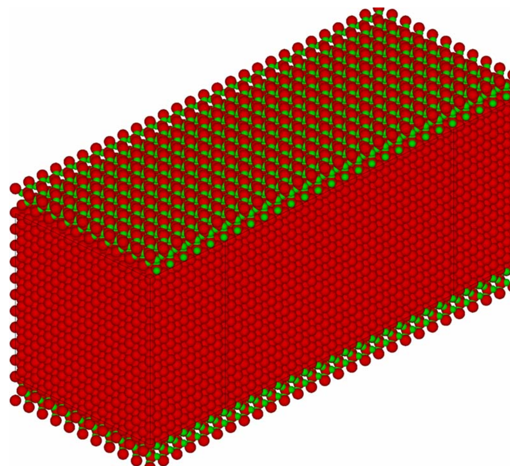

FIG. 1. (Color online) An illustration for the idealized atomic structure of a 10-nm-gate-length Si DG-MOSFET. The red (dark gray) spheres represent Si atoms while the green (light gray) ones represent oxygen atoms of the oxide layer.

*manuelxx@usc.es

 ©2008 The American Physical Society

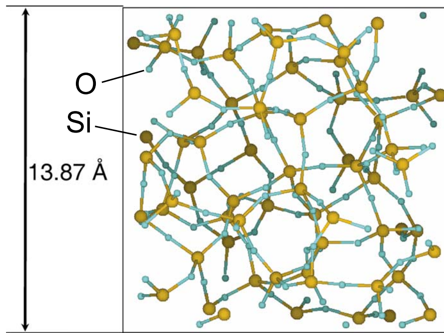

FIG. 2. (Color online) Amorphous SiO_2 structure of 192 atoms (ρ=2.39 g/cm^{-3}) obtained from classical molecular dynamics simulations [7].

with α-quartz SiO_2 dielectric layer and (ii) a silicon semiconductor with the monoclinic HfO_2 on the top of an α-quartz SiO_2 layer. These material systems are typically fabricated in current transistors. This paper is organized as follows. Section II presents the meshing strategy used to handle crystalline regions. Section III describes a methodology to include gate dielectrics with noncrystalline structure. This is followed by the results concerning tetrahedral quality presented in Sec. IV. A refinement algorithm for the generated meshes is discussed in Sec. V, followed by two application examples of the mesh generation strategy presented in Secs. VI and VII. Finally, concluding remarks are drawn in Sec. VIII.

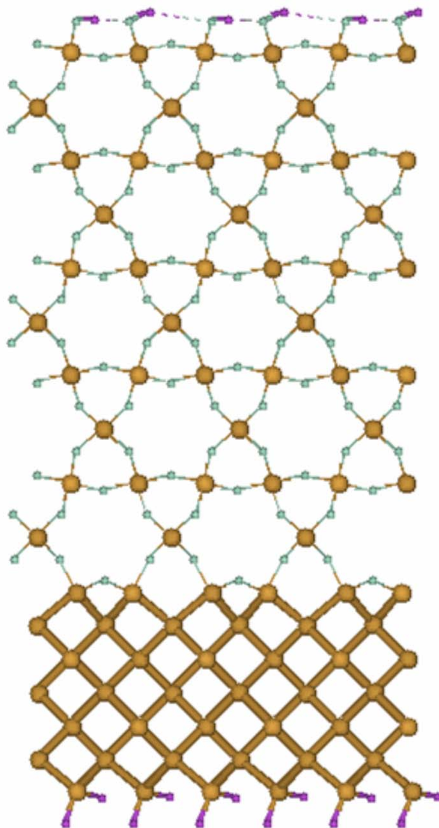

FIG. 3. (Color online) Atomic structure of a crystalline Si/SiO_2 interface passivated by hydrogen [8].

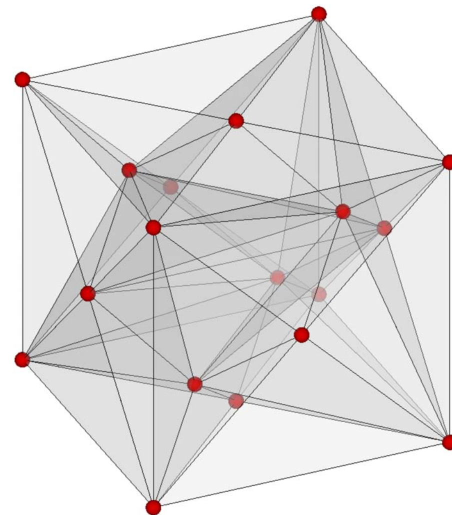

FIG. 4. (Color online) Mesh of the terminal octant using the atoms in the unit cell of Si as nodes.

II. MESHING APPROACH FOR CRYSTALLINE REGIONS

In this section, we describe the meshing strategy accounting for the actual atomic positions in the semiconductor device. Recently, Delaunay meshes [9] with nodes in the position of the atoms have been employed in simulations of nanowire transistors [10,11], but only the atoms of the Si lattice have been considered, ignoring the position of the atoms of the oxide layers and transition regions. However, Delaunay algorithms may have problems when applied to quasicrystalline regions resulting from the inclusion of a crystalline oxide and interfaces. This is mainly due to an excessive generation of sliver tetrahedra, which requires a post-processing in order to achieve acceptable mesh quality. Furthermore, it is advantageous to use constrained triangulations in order to retain particular crystalline planes of the structure. This can be useful to define interface properties and to impose boundary conditions in subsequent simulations.

We have chosen a method based on an octree algorithm [12,13] with unit cells of materials as terminal octants and the possibility to utilize different decomposition schemes in the same mesh. As a first step, tetrahedra decomposition schemes for the extended unit cells of the materials in the structure must be defined. These extended unit cells (unit cells from now on) include extra dummy atoms in order to complete a volume which covers the full space when it is replicated, but they will be removed later in the replication process. The decomposition of the unit cells into tetrahedra can be carried out in different ways, the only requirement being the symmetry in the surface of opposite faces so that we obtain a conformal mesh in the process of replication. In Figs. 4 and 5 we show, as an example, the decomposition of the unit cells of silicon (Si) and crystalline silicon dioxide (α-SiO_2). In the case of Si, we have used the internal symmetry of the unit cell to carry out the decomposition, tetrahedralizing a triangular prism and replicating it 3 times with the corresponding symmetry transformations. An example of the mesh in a silicon slab of $31\times19\times12$ unit cells con-

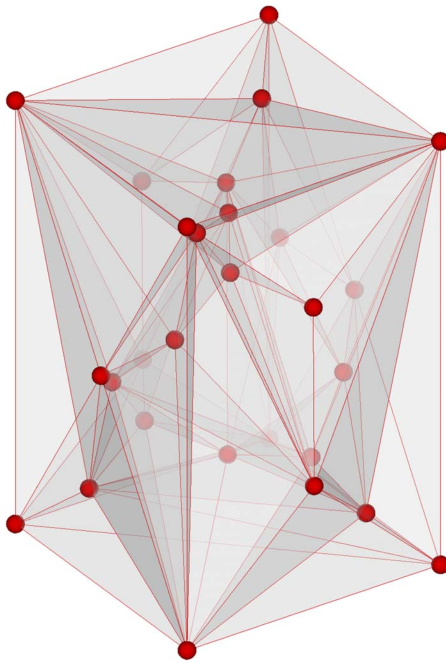

FIG. 5. (Color online) Pattern used to build the mesh of crystalline SiO_2 using nodes in the atomic positions.

structed using the described tetrahedra decomposition scheme can be seen in Fig. 6.

A second step must be the decomposition of the periodic structure at the interface between different materials—e.g., the Si/SiO_2 interface. Such a decomposition cannot be done simply using the bulk crystalline structures of corresponding materials because of the deformation of their local atomic structure at the interface. We have adopted the topology of this interface from Ref. [8], while the local atomic structure of the interface has been obtained using density functional theory (DFT) calculations as described in Ref. [14]. An example of the decomposition of an interface cell is shown in Fig. 7 for the Si/SiO_2 interface. Note that the upper part of the decomposition of the cell is the same as that shown in Fig. 5, but the bottom part, the interface between Si and α-quartz, is different.

Now that we have the basic units to build the mesh, we can proceed to the definition of the structure we want to

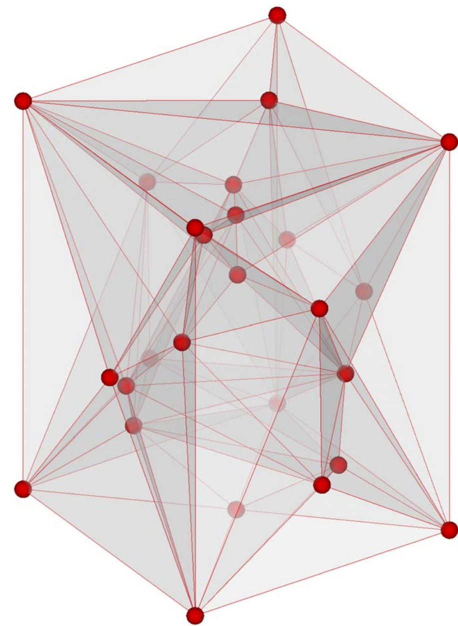

FIG. 7. (Color online) Pattern used to build the mesh of the interface between crystalline SiO_2 and crystalline Si.

mesh. This includes the specification of materials and approximate dimensions of different layers. The information is used to obtain the number of unit cells per material to be replicated in each direction, which is done in the next step. We have to take into account that a material layer could have zero width if the specified dimension is too small. In this case, the whole width of the region would be assigned to the interface. Once the mesh of the materials with the given dimensions is built, the displacement of the nodes is carried out in order to match the actual relative positions of atoms.

The final step in building the mesh is the introduction of the interfaces, which always have only one layer to join the materials above and below. The coordinates of the nodes are displaced directly according to the mesh of the materials they are interfacing. Figure 8 shows an example of the mesh constructed using the described technique for a $SiO_2/Si/SiO_2$ structure. The relaxed atomistic structure of the Si/SiO_2 interface has been obtained from first-principles calculations [8] using DFT. Figure 9 shows another example of our methodology applied to a $Si/SiO_2/HfO_2$ structure.

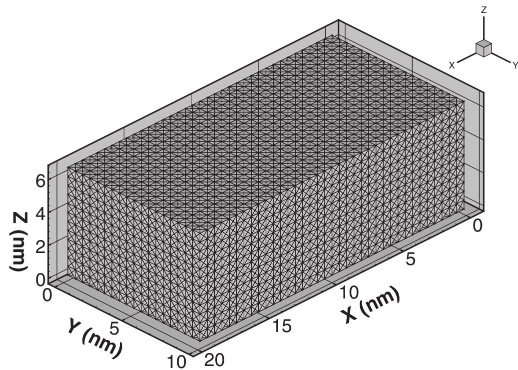

FIG. 6. Surface of the mesh of a Si slab approximately 6.5 nm thick.

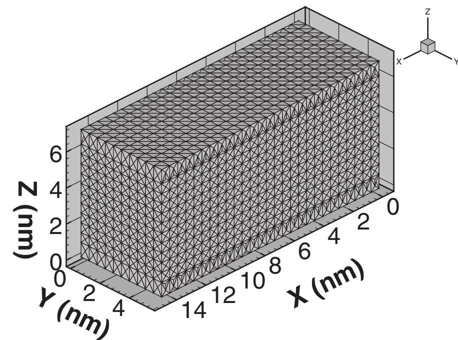

FIG. 8. Mesh of a DG-MOSFET with crystalline SiO_2 as gate dielectric using patterns.

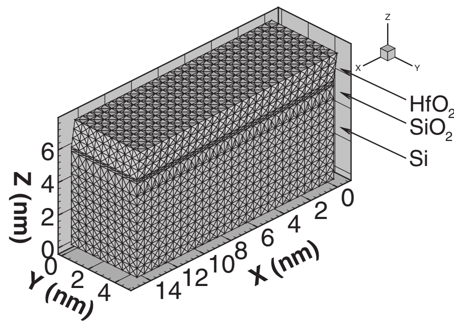

FIG. 9. Mesh of a MOSFET with gate dielectric composed of one layer of crystalline SiO_2 and monoclinic HfO_2.

Again, the SiO_2/HfO_2 interface was extracted from the atomic distribution obtained using first-principles calculations [15] shown in Fig. 10. In this case, the growth of the monoclinic HfO_2 at the top of Si/SiO_2 structure did not produce a crystalline interface. However, it still had some patterns which we extracted in order to obtain the cell which represents the interface. With this modification, the obtained mesh does not replicate exactly the initial atom positions. However, in the next section we present a technique to modify these crystalline meshes, making them closer to the real structures.

A final difficulty, which must be addressed building the atomic resolution meshes, is the difference between the lattice constants of the materials forming the layered structure. When a crystalline material is grown on top of another crystalline material with a different lattice constant, two situations may appear [16] (see Fig. 11).

(i) If the thickness of the grown material is below the critical thickness, then its lattice constant, provided that the lattice mismatch is small, is modified to match that of the other material.

(ii) If the thickness of the grown material is above the critical thickness, then the lattice constant remains unchanged and dislocations appear.

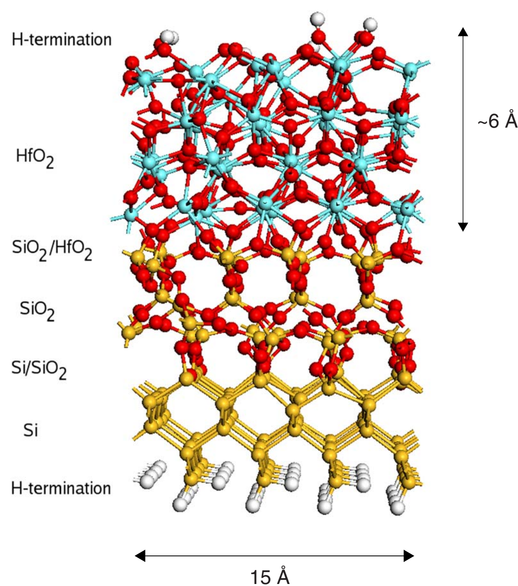

FIG. 10. (Color online) Calculated atomic structure of a $Si/SiO_2/HfO_2$ interface.

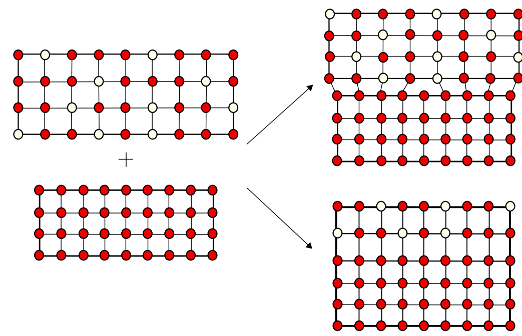

FIG. 11. (Color online) Possible growth of two different crystalline materials. Depending on the thickness of the layer, the resulting structure can be strained (bottom) or dislocated (top).

As the first approximation we suppose that the crystalline oxide layer is thin enough to fall into the first group. A crystal of the oxide layers with the dimensions of Si in the plane parallel to the interface is therefore created. Although this is the most usual situation in semiconductor device structures, it would also be possible to introduce a generalized cell at the interface which allows us to study materials with higher mismatches between their lattice constants.

III. MESHING OF AMORPHOUS LAYERS

In the previous section, we have shown how our mesh generation strategy creates meshes for crystalline materials. However, in actual devices, the dielectric layer is usually amorphous. This requires an extension of the mesh generator to allow the handling of amorphous structures.

The description of the structure of amorphous materials and their interfaces is a very complex subject not completely understood yet even for an extensively used material as SiO_2 [17], whose interface with Si has been the key for the success of CMOS technology. The generation of realistic Si/SiO_2 interface structures requires the use of computational techniques such as DFT and classical molecular dynamics simulations [17–20] and is beyond the scope of this work.

As a first approximation to the problem, we will accomplish a local transformation of the mesh in order to remove the crystallinity in the location of the nodes of the oxide to mimic an amorphous node distribution. This can be used to study qualitatively the impact of the random variations of the material properties in the amorphous layer on the device behavior. However, this transformation results in atom distributions whose physical properties such as the distribution of bond angles do not match the experimental ones. Further work should include the inclusion of amorphous oxides and interfaces from first-principles simulation data.

The main idea of the algorithm is the formation of an amorphous material layer from the crystalline one we have meshed already with the previously described algorithm. We also would like to keep the same adjacency graph for the mesh to be able to use the same data structures in the simulator, speeding up the simulation of microscopically different devices.

The algorithm implemented performs an adjustable randomization of the positions of the nodes of the original mesh.

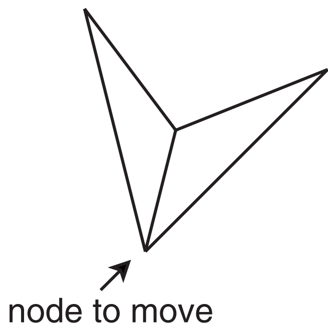

FIG. 12. Two triangles delimiting a nonconvex surface.

The degree of allowed displacement of the nodes is given by a parameter $\beta \in (0,1]$. A value near zero means that the allowed movement is very small, whereas a value of 1 specifies a movement in the whole allowed volume. To avoid intersections between tetrahedra when moving nodes we define the allowed volume in two steps. In the first step we make a list of the neighbor tetrahedra. They define a volume surrounding completely the target node. If this volume is convex, then it is the volume where the node can be freely moved without any need to change connectivities. If the volume is not convex, then we have to restrict the volume to avoid intersections. Figures 12 and 13 show an example of nonconvex mesh elements and their adjustment, respectively, in two dimensions.

In three dimensions the situation is equivalent, but we have to restrict the movement using planes instead of straight lines. We also have to take into account that a node may belong to an arbitrary number of tetrahedra, thus defining an arbitrary polyhedron. Hence, the valid volume to move the node will be arbitrary and difficult to define in terms of the tetrahedra containing this given node. Therefore, we have decided to use a rejection technique to generate the final position of the node. First, we generate an arbitrary point in the whole volume defined by the neighbor tetrahedra using a uniform distribution. If the vector defined by the old and new positions of the node do not cross any of the planes defined by all the opposite faces to that node, we keep the change; otherwise, we generate a new random candidate. In this way we obtain a random movement in the valid volume with uniform probability. Running the randomizing function several times, we get different amorphous layers from the same crystalline structure. Figures 14 and 15 show one mesh generated with this method and the representation of its corresponding atoms, respectively.

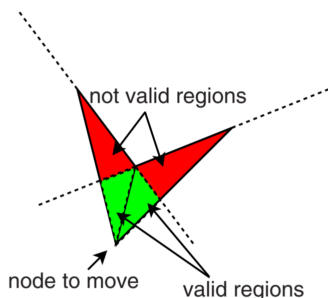

FIG. 13. (Color online) Regions of the surface which can and cannot be used to move the node.

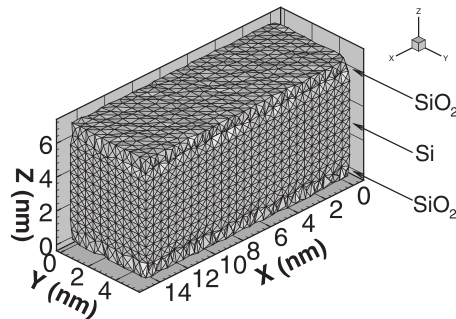

FIG. 14. Mesh with amorphous regions obtained from the mesh of the crystalline materials.

IV. MESH QUALITY

The characteristics of the systems of equations that describe the discretized partial differential equations which must be solved strongly depend on the properties of the mesh. However, the optimal mesh is problem dependent, so a universal mesh quality criterion cannot be defined. Therefore, we have used an element quality criterion satisfying the definition proposed in Ref. [21]. The *aspect ratio* γ, defined as

$$\gamma = \frac{12}{\sqrt{6}} \frac{r_{in}}{\max_{i,j} l_{ij}}, \tag{1}$$

where r_{in} is the radius of the inscribed sphere and l_{ij} (l_{01}, l_{02}, l_{03}, l_{12}, l_{13}, l_{23}) are the tetrahedron edge lengths, has been selected as a quality shape measure. The aspect ratio γ provides a maximum value of 1 in the case of a regular tetrahedron. The value of the aspect ratio is zero for any degenerate tetrahedron (coplanar nodes). To calculate the in-radius r_{in}, we use the following formula:

$$r_{in} = \frac{3v}{\sum_{i=0}^{3} s_i}, \tag{2}$$

where v is the volume of the tetrahedron and s_i the areas of each face of the tetrahedron.

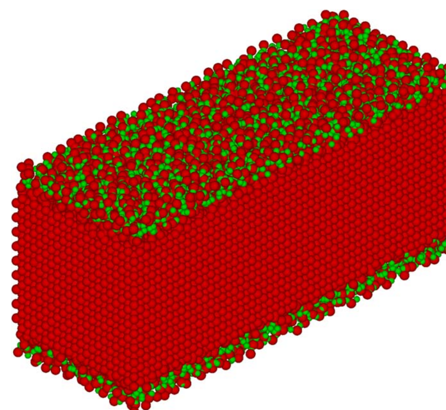

FIG. 15. (Color online) Atoms in the structure after the process to make the oxide amorphous. Red (dark gray) spheres represent silicon atoms and green (light gray) spheres oxygen atoms. Note the irregular positions of atoms in the oxide layer as compared to their regular positions in Fig. 1.

TABLE I. Parameters describing quality distributions of the tetrahedra for the meshes of different materials. The parameters given for the amorphous meshes are $\beta_1=0.05$ and $\beta_2=1.0$.

Material	$\langle\gamma\rangle$	σ	N_{AC}	γ_{max}	γ_{min}
Si	0.51	0.08	1.031	0.662	0.458
SiO_2	0.31	0.09	0.399	0.553	0.151
HfO_2	0.46	0.12	−0.089	0.777	0.200
Si-SiO_2	0.39	0.12	0.789	0.739	0.183
SiO_2-HfO_2	0.40	0.10	−0.838	0.575	0.127
a-SiO_2 (β_1)	0.31	0.09	0.372	0.595	0.132
a-SiO_2 (β_2)	0.29	0.12	0.789	0.845	0.102

Table I presents parameters characterizing the distributions of γ for the different unit cells, including the average aspect ratio ($\langle\gamma\rangle$), standard deviation (σ), asymmetry coefficient (N_{AC}) , and maximum and minimum aspect ratios (γ_{max} and γ_{min} respectively).

To avoid highly malformed elements, the movement of the nodes in the amorphous mesh generation includes a second constraint related to the quality. The new position of a node cannot produce any tetrahedron with aspect ratio lower than a given value. Although high values of the threshold would be ideal from the mesh quality point of view, a tradeoff is required since too high values could make the generation too slow or even impossible.

V. MESH REFINEMENT

The unstructured meshes described so far may not have enough resolution in regions with very sharp variations of some physical quantity. Local mesh refinement will be needed, for example, to include a more realistic description of the charge density profile for ionized impurities obtained from first-principles calculations [7].

Our goal is to refine the mesh in selected regions while maintaining the underlying structure of the atomic lattice. To accomplish this task of mesh refinement, we have chosen a bisection algorithm [22–24] which includes new nodes (one at a time) in the mesh on selected edges. Figure 16 shows an example of such refinement where the tetrahedron $T_0=\{N0,N1,N2,N3\}$ is divided into two new tetrahedra $T_1=\{N0,N',N2,N3\}$ and $T_2=\{N',N1,N2,N3\}$. In our implementation of the algorithm, we split all the tetrahedra sharing the edge instead of maintaining the conformality of the mesh in a subsequent step. The selection of the edge to bisect can be made by using different criteria. We choose a threshold for a given quantity (a physical one or any mathematical construction such as the residual) and tetrahedra with values over this threshold are selected for the refinement. A search in the given tetrahedron is then carried out to choose the edge to split. This is again based on nodal values of particular quantity. Neighbor tetrahedra are checked to give a preference to edges with higher values of this refinement variable. Figure 17 shows an example of a mesh near an ionized impurity refined using the potential profile as a guide.

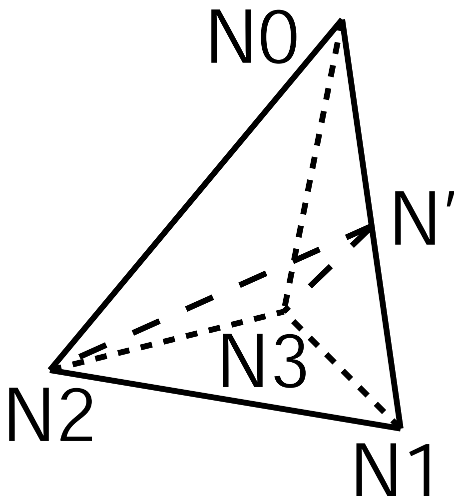

FIG. 16. Refinement of a tetrahedron using bisection.

VI. APPLICATION EXAMPLE: RANDOM DOPANTS

As an example of the use of the “atomistic” meshes, we present a study of the impact of random dopants on the I_D-V_G characteristics of a 10-nm-gate-length DG thin-body Si MOSFET (Fig. 18) using drift-diffusion simulations. In this model we have to solve the Poisson and current continuity equations with mixed Dirichlet and Neumann boundary conditions. The discretization of the Poisson equations has been carried out using the Ritz-Galerkin approximation with

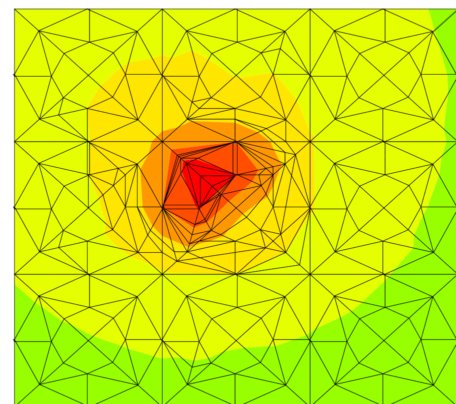

FIG. 17. (Color online) Detail of the refinement near one impurity atom. Colors correspond to a potential contour.

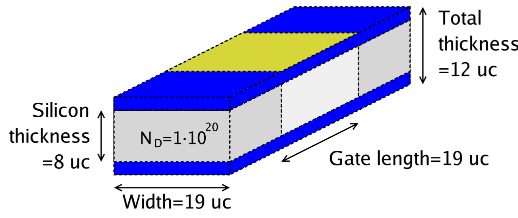

FIG. 18. (Color online) Geometry of the simulated 10-nm-gate-length double-gate MOSFET. Dimensions are in units of the Si unit cell (1 unit cell=0.543 nm).

linear finite-element basis functions [25]. On the other hand, the discretization of the continuity equations requires a special approach. In particular, the Scharfetter-Gummel discretization scheme has been used in this work [25]. The resulting system of equations is decoupled using a Gummel scheme and linearized using the Newton method [26]. To solve these linear systems, we have used an standard ILUT preconditioner combined with an FGMRES solver [27]. More details about the simulator and the numerical methods employed can be found in [28].

The previously described meshing approach is employed to create an atomistic, high-quality mesh for the Si body of the transistor (Fig. 6). Then, a Monte Carlo approach is used to place dopants by replacing silicon atoms, thus creating a particular distribution of random dopants following the continuous doping distribution [4]. Each random dopant distribution produces a unique potential profile, an example of which is shown in Fig. 19.

First, we compare the results obtained with the atomistic mesh and the results obtained with a very fine nonatomistic mesh. The results of the simulations of the device with continuous doping are shown in Fig. 20. This confirms that the atomistic mesh is able to accurately capture the variations in the physical quantities. Figure 20 also shows the simulated I_{D}-V_{G} characteristics of the whole ensemble of DG MOSFETs with 10 nm gate length at a drain voltage of 0.05 V. There is a significant spread of the curves, reflected in the standard deviation of the threshold voltage, σV_T=0.005 V. In addition, an impact of the fluctuations on the on-current has been also investigated. Figure 21 shows the normalized standard deviation of the drain current as a function of the gate bias at a low drain bias. The exponential-like behavior of the current as a function of the gate bias in the subthreshold region results in a large (more than 35%) impact of the

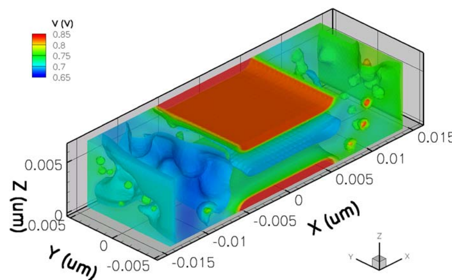

FIG. 19. (Color online) Electrostatic potential for a drain bias of 0.05 V and a gate bias of 1.1 V for one configuration of the dopants located at atomic positions.

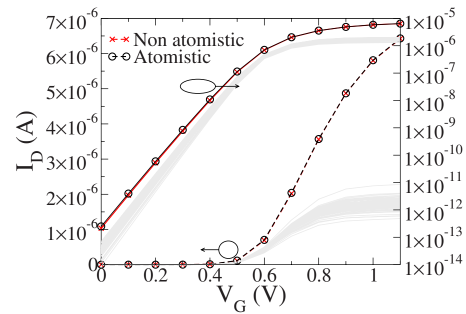

FIG. 20. (Color online) I_{D}-V_{G} characteristics at a drain voltage of 0.05 V for an ensemble of simulated transistors. The drain current obtained using continuous doping with the nonatomistic (crosses) and atomistic (circles) meshes are highlighted.

random dopants. The fluctuations are diminishing with the increasing gate bias above the threshold voltage when the current is in the Ohmic regime and then saturates. In the subthreshold region, it is common to express a spread in the drain current from the distribution of $\log_{10}(I_D)$ which gives a standard deviation of $\sigma \log_{10}(I_D) \simeq 0.17$. At a high gate voltage, the relative dispersion of the results, $\sigma I_D \simeq 10\%$, is lower as shown in Fig. 21. Similarly, the difference between the average drain current obtained from the ensemble of simulations with the atomistically described source and drain and the current obtained from a simulation using a continuous doping in the source and drain becomes smaller at a high gate voltage as can be seen in Fig. 22.

The large difference between the continuous and the average current in the atomistic simulations is due to the trapping of charge in the sharply resolved Coulomb wells associated with the individual donors. This is a drawback of the drift-diffusion approach which assumes either Boltzmann or Fermi-Dirac statistics and therefore heavily populates the wells. In the same time the ground state in the wells is very close to the conduction band edge and the heavy trapping inherent to the drift-diffusion approach is physically unrealistic. This drawback of the drift-diffusion simulations can be remedied by the introduction of density gradient quantum corrections [29]. The large variation of the on current in our simulation is a reflection of this artifact.

We have also compared the simulations of devices with atomistic doping using the atomistic and nonatomistic meshes. After simulating the ensemble of devices with the

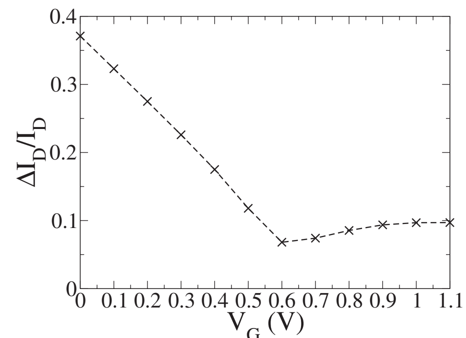

FIG. 21. Normalized standard deviation of the current as a function of the gate voltage for a drain bias of 0.05 V.

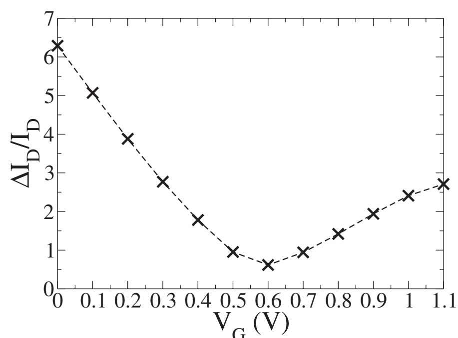

FIG. 22. Relative variation of the drain current for a drain bias of 0.05 V.

atomistic mesh, we chose the configuration of random dopants exhibiting the highest and lowest currents. The devices were then simulated using two different charge assignment schemes on the nonatomistic mesh: (i) assigning charge of the dopant to the nearest node in the mesh [so-called *nearest grid point* (NGP) scheme] [30] and (ii) splitting the charge among all the neighboring nodes [so-called *cloud-in-cell* (CIC) scheme] [30]. The results of such simulations are shown in Fig. 23. First, we can see the improvement in the convergence when using the atomistic mesh. The configuration of dopant atoms which produces the minimum current did not converge when using the nonatomistic mesh (uniform structured tetrahedral mesh) for the NGP charge assignment scheme. However, the simulations using the other configuration of dopants give very similar results when using both the atomistic and nonatomistic (using NGP) meshes. This is expected due to the very fine nonatomistic mesh, since the distance between two nodes is small enough to minimize the correlation between dopant positions introduced by the charge assignment scheme. The discrepancy with the nonatomistic mesh using CIC charge assignment is a consequence of a different charge trapping in the nodes originating from the different potential profiles in the vicinity of the ionized impurities [29] (discussed in the previous paragraph) which makes a fair comparison complicated.

VII. APPLICATION EXAMPLE: TRANSITION LAYERS

As a second example, we present a study of the impact of the transition region between Si and SiO_2 on the transport

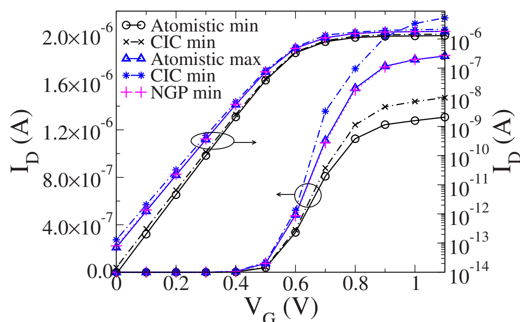

FIG. 23. (Color online) I_D-V_G characteristics for the devices showing the lowest (min) and highest (max) currents using the atomistic mesh and the uniform mesh with two different charge assignments: cloud-in-cell (CIC) and nearest grid point (NGP) schemes.

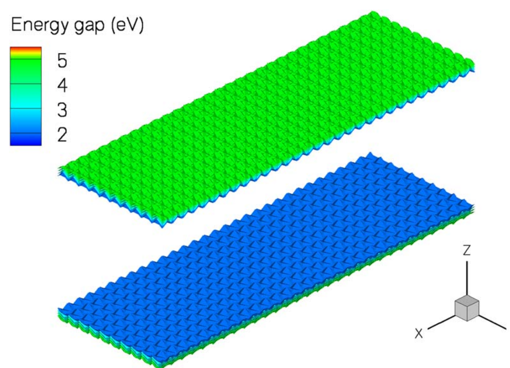

FIG. 24. (Color online) Isosurfaces of the energy band gap in the transition region of SiO_2.

characteristics of a 6-nm-gate-length DG thin-body Si MOSFET with a nominal oxide thickness of 8 Å. The change of the atomic structure at the Si/SiO_2 interface leads to the existence of electronic states close to the conduction band of the Si, producing a gradual transition of the band gap and the permittivity inside the SiO_2 [31,32]. Although the impact of this transition region on the characteristics of MOS inversion layers has been previously studied [33–35], little work has been done to study the influence on the drain current of MOSFETs.

The band gap is obtained from the projected density of states (PDOS) calculated using DFT simulations and then scaled to match the measured values of the energy band gap for the bulk materials. On the other hand, the value of the permittivity is assumed to change linearly in the transition region. Figure 24 shows band-gap isosurfaces in the transition layer of the oxide, showing its variation with the atomic position.

After obtaining the new values of the band gap and the permittivity, we evaluate the impact of the transition regions in the top and bottom interfaces on the I_D-V_G characteristics of the DG MOSFET. Figure 25 shows the results in both linear and logarithmic scales for two devices, the one with abrupt interfaces and the one with a transition region. We observe an improvement in the characteristics of the device when we include the transition region. The device exhibits a better subthreshold slope and also a higher on-current. Further simulations showed that this effect is mainly due to the transition in the permittivity and that, at least with our simu-

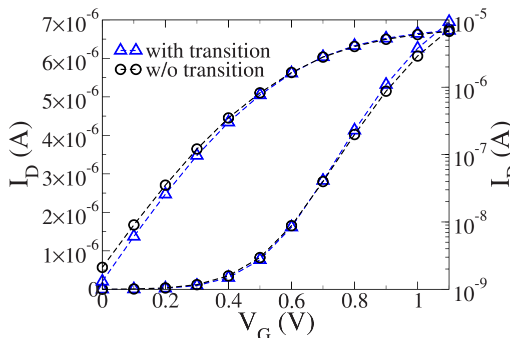

FIG. 25. (Color online) I_D-V_G characteristics for the devices with realistic and abrupt interfaces.

lation model, the effect of the transition in the band gap is almost negligible.

VIII. CONCLUSION

We have presented a strategy to build high-quality meshes for nanoscaled CMOS devices with nodes in the positions of the atoms constituting the device. Such atomic meshes, for example, precisely describe the dopant positions in the Si crystal lattice and can be used to study correlation effects or doping clustering. The method can be also used to represent accurately atomic-scale interface roughness. This is specially important for nanoscale transistors since the interatomic distances are comparable to the dimensions of the device. More precisely, the exact positions of the atoms have to be taken into account to obtain a realistic representation of physical quantities such as potential, charge, and/or wave functions in order to carry out the accurate modeling of carrier transport. We have illustrated our approach with two examples. In the first example, an ensemble of devices with discrete and microscopically different doping distributions has been simulated. In the second example, the effect of the nonabrupt Si/SiO_2 interface on the drain current has been studied. We have also described the adaptive mesh refinement algorithm which can be used to accurately resolve potential, charge, and/or current distributions in the vicinity of individual dopants. Finally, we have described how our mesh generation scheme can be extended to describe pseudoamorphous layers which play an essential role at a semiconductor/dielectric interface.

ACKNOWLEDGMENTS

This work was supported by the Spanish Government (MCYT), Project No. TIN2004-07797-C02, and by HPC-EUROPA (Grant No. RII3-CT-2003-506079). M.A. thanks Ministerio de Educación y Ciencia de España for support (FPU), while K.K. and P.V.S. thank the UK EPSRC (Grant No. EP/D070236/1) and Japan MEXT (Grant No. 16GS0205), respectively, for support.

[1] K. E. Drexler, *Nanosystems: Molecular Machinery, Manufacturing, and Computation* (Wiley, New York, 1992).
[2] http://www.itrs.net
[3] J. Cervenka, W. Wessner, E. Al-Ani, T. Grasser, and S. Selberherr, IEEE Trans. Comput.-Aided Des. **25**, 2118 (2006).
[4] A. Asenov, IEEE Trans. Electron Devices **45**, 2505 (1998).
[5] D. Frank, IBM J. Res. Dev. **46**, 235 (2002).
[6] A. R. Brown, A. Asenov, and J. Watling, IEEE Trans. Nanotechnol. **1**, 195 (2002).
[7] S. Mukhopadhyay, P. V. Sushko, A. M. Stoneham, and A. L. Shluger, Phys. Rev. B **70**, 195203 (2004).
[8] T. Yamasaki, C. Kaneta, T. Uchiyama, T. Uda, and K. Terakura, Phys. Rev. B **63**, 115314 (2001).
[9] Q. Du and D. Wang, J. Comput. Appl. Math. **195**, 8 (2006).
[10] M. Luisier, A. Schenk, and W. Fichtner (unpublished).
[11] M. Luisier, A. Schenk, and W. Fichtner, Appl. Phys. Lett. **90**, 102103 (2007).
[12] M. Aldegunde, J. J. Pombo, and A. J. García-Loureiro, Int. J. Numer. Model. **19**, 473 (2006).
[13] N. Hitschfeld-Kahler, Eng. Comput. **21**, 101 (2005).
[14] L. Giordano, P. V. Sushko, G. Pacchioni, and A. L. Shluger, Phys. Rev. B **75**, 024109 (2007).
[15] J. L. Gavartin and A. L. Shluger, Microelectron. Eng. **84**, 2412 (2007).
[16] J. S. Yuan, *SiGe, GaAs, and InP Heterojunction Bipolar Transistors* (Wiley, New York, 1999).
[17] D. Fischer, A. Curioni, S. Billeter, and W. Andreoni, Appl. Phys. Lett. **88**, 012101 (2006).
[18] A. Pasquarello, M. S. Hybertsen, and R. Car, Phys. Rev. B **53**, 10942 (1996).
[19] R. Buczko, S. J. Pennycook, and S. T. Pantelides, Phys. Rev. Lett. **84**, 943 (2000).
[20] A. Bongiorno and A. Pasquarello, Appl. Phys. Lett. **83**, 1417 (2003).
[21] J. Dompierre, P. Labbé, F. Guibault, and R. Camarero, in *Proceedings of the 7th International Meshing Roundtable* (Sandia National Laboratories, Dearborn, Michigan, 1998), pp. 459–478.
[22] M.-C. Rivara, SIAM J. Numer. Anal. **21**, 604 (1984).
[23] D. N. Arnold, A. Mukherjee, and L. Pouly, SIAM J. Sci. Comput. **22**, 431 (2000).
[24] W. Wessner, J. Cervenka, C. Heitzinger, A. Hossinger, and S. Selberherr, IEEE Trans. Comput.-Aided Des. **25**, 2129 (2006).
[25] P. A. Markowich, *The Stationary Semiconductor Device Equations* (Springer-Verlag, Wien, 1986).
[26] R. E. Bank and D. J. Rose, Numer. Math. **37**, 279 (1981).
[27] Y. Saad, *Iterative Methods for Sparse Linear Systems* (PWS, Boston, Massachusetts, 1996).
[28] A. J. García-Loureiro, K. Kalna, and A. Asenov, Int. J. Numer. Model. **18**, 327 (2005).
[29] G. Roy, A. R. Brown, F. Adamu-Lema, S. Roy, and A. Asenov, IEEE Trans. Electron Devices **53**, 3063 (2006).
[30] R. W. Hockney and J. W. Eastwood, *Computer Simulation Using Particles* (IOP, Bristol, 1988).
[31] C. Kaneta, T. Yamasaki, T. Uchiyama, T. Uda, and K. Terakura, Microelectron. Eng. **48**, 117 (1999).
[32] F. Giustino and A. Pasquarello, Phys. Rev. B **71**, 144104 (2005).
[33] F. Stern, Solid State Commun. **21**, 163 (1977).
[34] H. Watanabe, D. Matsushita, and K. Muraoka, IEEE Trans. Electron Devices **53**, 1323 (2006).
[35] S. Markov, N. Barin, C. Fiegna, S. Roy, E. Sangiorgi, and A. Asenov, in *Proceedings of the 12th International Conference on Simulation of Semiconductor Processes and Devices*, edited by T. Grasser and S. Selberherr (Springer-Verlag, Wien, 2007), pp. 149–152.